Title

Engineering Embden—Meyerhof—Parnas Glycolysis to Generate Noncanonical Reducing Power

Journal

ACS Catalysis, 12(14)

ISSN

2155-5435

Authors

King, Edward

Cui, Youtian

Aspacio, Derek

et al.

Publication Date

2022-07-15

DOI

10.1021/acscatal.2c01837

Peer reviewed

HHS Public Access

Author manuscript

ACS Catal. Author manuscript; available in PMC 2023 August 24.

Published in final edited form as:

ACS Catal. 2022 July 15; 12(14): 8582–8592. doi:10.1021/acscatal.2c01837.

Engineering Embden–Meyerhof–Parnas Glycolysis to Generate Noncanonical Reducing Power

Edward King[¶],
Department of Molecular Biology and Biochemistry, University of California, Irvine, Irvine, California 92697-3900, United States

Youtian Cui[¶],
Genome Center, University of California, Davis, Davis, California 95616, United States

Derek Aspacio[¶],
Department of Chemical and Biomolecular Engineering, University of California, Irvine, Irvine, California 92697-3900, United States

Frances Nicklen,
Department of Biomedical Engineering, University of California, Irvine, Irvine, California 92697-3900, United States

Linyue Zhang,
Department of Chemical and Biomolecular Engineering, University of California, Irvine, Irvine, California 92697-3900, United States

Sarah Maxel,
Department of Chemical and Biomolecular Engineering, University of California, Irvine, Irvine, California 92697-3900, United States

Ray Luo,
Department of Molecular Biology and Biochemistry, Department of Chemical and Biomolecular Engineering, and Department of Biomedical Engineering, University of California, Irvine, Irvine, California 92697-3900, United States

Justin B. Siegel,
Department of Chemistry, Genome Center, and Department of Biochemistry and Molecular Medicine, University of California, Davis, Davis, California 95616, United States

Corresponding Authors: Erick Aitchison – *Department of Molecular Biology and Biochemistry, University of California, Irvine, Irvine, California 92697-3900, United States*; drewa1c@msn.com, Han Li – *Department of Chemical and Biomolecular Engineering and Department of Biomedical Engineering, University of California, Irvine, Irvine, California 92697-3900, United States;* han.li@uci.edu.

[¶]E.K., Y.C., and D.A. contributed equally.

Author Contributions

E.K., D.A., and H.L. designed the experiments. Y.C. and E.K. performed Rosetta modeling. E.A. performed the molecular dynamics and the shortest pathway network analysis. E.K., F.N., and L.Z. performed the rational protein engineering experiments. E.K., F.N., and L.Z. performed the Michaelis–Menten kinetic experiments for cofactors. D.A. performed kinetic analysis for D-G3P. S.M. constructed the strains. D.A. performed growth studies. E.K., E.A., Y.C., R.L., and J.S. analyzed the modeling results. All authors analyzed the data and wrote the manuscript.

The authors declare no competing financial interest.

Complete contact information is available at: https://pubs.acs.org/10.1021/acscatal.2c01837

Erick Aitchison,
Department of Molecular Biology and Biochemistry, University of California, Irvine, Irvine, California 92697-3900, United States

Han Li
Department of Chemical and Biomolecular Engineering and Department of Biomedical Engineering, University of California, Irvine, Irvine, California 92697-3900, United States

Abstract

Noncanonical cofactors such as nicotinamide mononucleotide (NMN^+) supplant the electron-transfer functionality of the natural cofactors, $NAD(P)^+$, at a lower cost in cell-free biomanufacturing and enable orthogonal electron delivery in whole-cell metabolic engineering. Here, we redesign the high-flux Embden–Meyerhof–Parnas (EMP) glycolytic pathway to generate NMN^+-based reducing power, by engineering *Streptococcus mutans* glyceraldehyde-3-phosphate dehydrogenase (*Sm* GapN) to utilize NMN^+. Through iterative rounds of rational design, we discover the variant GapN Penta (P179K-F153S-S330R-I234E-G210Q) with high NMN^+-dependent activity and GapN Ortho (P179K-F153S-S330R-I234E-G214E) with ~3.4×10^6-fold switch in cofactor specificity from its native cofactor $NADP^+$ to NMN^+. GapN Ortho is further demonstrated to function in *Escherichia coli* only in the presence of NMN^+, enabling orthogonal control of glucose utilization. Molecular dynamics simulation and residue network connectivity analysis indicate that mutations altering cofactor specificity must be coordinated to maintain the appropriate degree of backbone flexibility to position the catalytic cysteine. These results provide a strategy to guide future designs of NMN^+-dependent enzymes and establish the initial steps toward an orthogonal EMP pathway with biomanufacturing potential.

GRAPHICAL ABSTRACT:

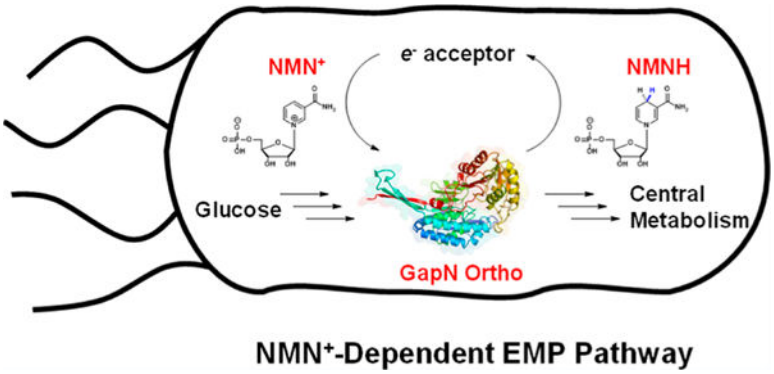

Keywords

Embden–Meyerhof–Parnas; Glycolysis; nicotinamide mononucleotide; noncanonical redox cofactor; computational protein design; orthogonal pathway engineering; glyceraldehyde-3-phosphate dehydrogenase

INTRODUCTION

Biomanufacturing applies engineered biological systems to synthesize fuels, commodities, and specialty chemicals from renewable resources. These processes often rely on the redox cofactors nicotinamide adenine dinucleotide [NAD(H)] or nicotinamide adenine dinucleotide phosphate [NADP(H)] to shuttle reducing energy. Large-scale usage of these natural redox cofactors is restricted by two key limitations: (1) they are expensive to use in cell-free biomanufacturing even when coupled with cofactor recycling[1–3] and (2) they are shared by numerous metabolic pathways native to the host in whole-cell biomanufacturing which prohibits direct transfer of reducing power to the desired reaction. A promising solution to overcome these challenges is to utilize structurally diverse noncanonical cofactors[4–9] such as nicotinamide mononucleotide (NMN^+), which maintain the electron-transfer functionality of natural cofactors and provide superior industrial advantages of faster mass transfer due to smaller sizes,[10] lower costs,[11,12] and importantly support for specific delivery of electron energy to targeted pathways as native enzymes are unable to utilize NMN(H).[13,14]

The Embden–Meyerhof–Parnas (EMP) pathway is the predominant route of feedstock uptake in most chassis organisms implemented in whole-cell-based biomanufacturing. In cell-free biomanufacturing, the EMP pathway has been efficiently reconstituted in vitro to reduce costs because it derives otherwise expensive cofactors and central metabolite building blocks from low-cost sugars.[15–19] Although we and others have previously engineered enzymes in alternative glycolytic routes including the Entner–Doudoroff (ED) pathway and pentose phosphate pathway (PPP) to recycle noncanonical cofactors,[12,13] EMP glycolysis has not been exploited to generate these unnatural forms of reducing power. In this work, we engineer *Streptococcus mutans* non-phosphorylating glyceraldehyde-3-phosphate dehydrogenase (*Sm* GapN)[20,21] to utilize NMN^+. *Sm* GapN converts D-glyceraldehyde-3-phosphate (D-G3P) to 3-phosphoglycerate (3-PG) without ATP production. Replacing the native phosphorylating glyceraldehyde-3-phosphate dehydrogenase (GapDH) in *Escherichia coli* with *Sm* GapN establishes an ATP-neutral EMP pathway for cell-free biomanufacturing which bypasses the need to balance ATP.[17,22] In vivo, an ATP-neutral EMP pathway is more thermodynamically favorable than the ATP-producing counterpart and has the potential to achieve high flux.[23] Because glycolytic flux is heavily regulated by the intracellular availability of NAD^+ and ATP,[24–28] an EMP pathway which is decoupled from both native redox cofactor and native energy currency will serve as a powerful tool to flexibly tune central metabolism independently of the cells' physiological states.

In this work, our design goals are twofold: for application in cell-free biomanufacturing, we aim to construct *Sm* GapN variants with a high catalytic efficiency and a high turnover rate using NMN^+; for application in whole-cell biomanufacturing, an orthogonal *Sm* GapN with minimal $NAD(P)^+$-dependent activity is required to specifically harvest electrons through EMP glycolysis in the form of NMNH to channel energy toward the desired downstream pathways. To achieve these goals, we performed multiple rounds of Rosetta modeling-guided rational design to iteratively increase NMN^+-dependent activity of *Sm* GapN and obtained the most active variant, GapN Penta (P179K-F153S-S330R-I234E-G210Q), with ~45-fold increased catalytic efficiency (k_{cat}/K_m) compared to the wild

type. The turnover rate (k_{cat}), which is a strong indicator of the catalyst's performance in cell-free systems where fast productivity is desirable and high cofactor concentration is achievable, improved by ~68-fold. In addition, we engineered GapN Ortho (P179K-F153S-S330R-I234E-G214E) with ~3.4×10^6-fold cofactor specificity switch from the enzyme's native cofactor $NADP^+$ to NMN^+, based on the catalytic efficiency compared to the wild type. GapN Ortho's activity toward both $NADP^+$ and NAD^+ is drastically reduced, enabling us to establish the first orthogonal EMP glycolysis in vivo with engineered *E. coli* where glycolytic flux is specifically dependent on NMN^+. Rosetta modeling of these variants' mechanisms reinforced our rational design principles of engineering NMN^+-specific enzymes by strengthening binding interactions with the NMN^+ phosphate group while excluding $NAD(P)^+$. However, this strategy faced a bottleneck where increasingly tight NMN^+ binding began to interfere with the precise protein conformational dynamics required for catalysis, as shown by experimental and molecular simulation results. Thus, this work also highlights the complementary nature of rational design and directed evolution in engineering noncanonical cofactor-dependent enzymes, where the latter is needed to yield compensatory mutations to restore protein dynamics that are not apparent through static structural models. The NMN^+-dependent GapN-coupled growth phenotype reported here will provide a foundation for implementing directed evolution of NMN^+-dependent activity.

RESULTS AND DISCUSSION

Rational Design of GapN to Enhance NMN^+-dependent Activity.

Initial rounds of rational design were based on constructing novel polar contacts to improve binding affinity for NMN^+. As a mononucleotide, NMN^+ lacks the canonical second nucleotide, exposing a single negatively charged phosphate at the location where the cofactor is truncated (Figure 1A). The native redox cofactor for GapN, $NADP^+$, contains a phosphorylated adenosine monophosphate (AMP) moiety that can engage in salt bridge or hydrogen bond formation with active site residues and enables favorable hydrophobic packing within the binding site (Figure 1B). These critical contacts include a hydrogen bond from the SER 231 hydroxyl to the AMP phosphate, ASP 215 forming a hydrogen bond to the adenosine amide, and a network of polar contacts surrounding the 2′ phosphate at LYS 177 and THR 180[21] (Figure 1B). The truncated cofactor NMN^+ lacks the AMP moiety and is unable to form these interactions; consequently, it binds with severely reduced affinity such that the specific activity is nearly undetectable at 1.8 ± 0.6 nmol min^{-1} mg^{-1} (Figure 1C).

We utilized Rosetta[29] to systematically simulate the effects of amino acid substitutions in the cofactor binding site on the predicted NMN^+ binding pose and affinity. During the simulation, all side chains within 6 Å of NMN^+ were allowed to be designed and any residues within 8 Å of the ligand were relaxed with backbone movements enabled. The obtained poses were sorted based on protein–ligand interface energy and total system energy, and the top scoring outputs were selected for further inspection and design.

Studies have revealed that the nicotinamide and ribose moiety of the cofactor must remain mobile during catalysis and adopt different binding poses during the acylation and hydride transfer steps.[30,31] We focused on strengthening interactions with the relatively static

phosphate group in NMN^+. Thus, we constructed the P179K variant (GapN 185), which showed an increase in specific activity to 18 ± 2 nmol min^{-1} mg^{-1} (Figure 1C). Rosetta modeling suggested that the lysine forms a salt bridge with the negatively charged phosphate groups (Figures S1 and 1D). This general approach of enhancing NMN^+-dependent activity has also been demonstrated with an NMN^+-dependent glucose dehydrogenase.[13]

For the second round of design, single mutations were introduced on top of GapN 185 and two variants showed gradual enhancement of NMN^+ specific activity: 19 ± 1 nmol min^{-1} mg^{-1} for P179K-F153S (GapN 187) and 24 ± 0.6 nmol min^{-1} mg^{-1} for P179K-S330R (GapN 193). Combination of all substitutions resulted in the triple mutant P179K-F153S-S330R (GapN Triple) which showed a synergistic increase to 68 ± 6 nmol min^{-1} mg^{-1}. Modeling suggests that both F153S and S330R form additional polar contacts latching onto the free phosphate group tail of NMN^+ (Figure 1D).

After the positions immediately surrounding the NMN^+ were exhausted, the third round of design explored second shell mutations that would support the engineered interactions with NMN^+ by reducing excess conformational entropy of binding residues. A quadruple mutant P179K-F153S-S330R-I234E (GapN Quad) was discovered with ~86 nmol min^{-1} mg^{-1} specific activity (Figure 1C). I234E is suggested to establish a salt bridge with P179K, locking the residue in place for the favorable contact with NMN^+ (Figure 1D). The fifth mutation producing variant P179K-F153S-S330R-I234E-G210Q (GapN Penta) showed further enhanced activity of 110 ± 5 nmol min^{-1} mg^{-1}. G210Q is modeled to reinforce positioning of I234E through a hydrogen bond (Figure 1D).

The above results are consistent with the hypothesis that NMN^+-dependent activity can continue to increase as more interactions are established between the enzyme and NMN^+. However, when an additional mutation I326K was introduced to form yet another salt bridge with the NMN^+ phosphate group, the activity decreased (Figure 1C). Kinetic analysis showed that the resulting variant GapN Hex (P179K-F153S-S330R-I234E-G210Q-I326K) has a ~2.4-fold decreased K_m compared to its predecessor, GapN Penta, consistent with stronger cofactor recognition by the enzyme as intended (Table 1, Figure 1E). Unexpectedly, $k_{cat}$for NMN^+ decreased substantially from 0.82 ± 0.1 s^{-1} for GapN Penta to 0.12 ± 0.01 s^{-1} for GapN Hex (Table 1), indicating suboptimal catalysis. GapN Hex presents complex epistatic relationships in which the effects of multipoint mutations cannot be easily predicted in a static model. There were also no large changes predicted in the enzyme backbone structure (Figure S2). Therefore, we next performed molecular simulations to investigate structural and dynamic changes involved in the full catalytic process.

Elucidation of Trade-off between Cofactor Binding and Turnover.

We first modeled the global backbone flexibility for each monomer of the tetrameric GapN assembly, which suggested that the high NMN^+-binding affinity variant GapN Hex became more rigid compared to wild type and the high turnover variant GapN Penta (Table 1, Figure S3). We next sought to evaluate (1) how do the mutations cause these changes in backbone flexibility and (2) how do these changes in flexibility impact catalysis?

Rosetta modeling provides rationale for the reshaped backbone flexibility by showing that the positively charged residues, S330R, I326K, and P179K in GapN Hex, directly interact with the phosphate of the NMN^+ molecule to secure it in the binding pocket (Figure 1D). These three sites are located at the opening of the binding pocket and extend from different domains of the protein.[20,21] Therefore, when NMN^+ is present, the different domains may be more tightly tied together resulting in altered global conformational dynamics. However, the answer to the second question is less apparent through this static model.

The turnover rate is strongly linked to the pre-organization of catalytic residues. Based on the mechanism for wild-type GapN, the catalytic CYS 284 performs a nucleophilic attack at the G3P aldehyde to generate the hemithioacetal intermediate.[32] Molecular dynamics simulations evaluating the trajectory of the tetrametric GapN assembly can reveal the influence of distal mutations in positioning this catalytically essential residue. Using the distance between the sulfur atom on CYS 284 and the alpha carbon of residue SER 450, which serves as a reference point in the cofactor binding pocket, we observed different positioning of CYS 284 for wild type, GapN Penta, and GapN Hex (Figure 2). The wild type demonstrates the preference for a 9–10 Å distance (CYS “in” state) for all monomers, which is characterized by adjacent positioning of CYS 284 by the 4-carbon of the nicotinamide moiety for immediate hydride transfer (Figure 2A). For monomer A in GapN WT, there is an additional state at 12 Å observed, which corresponds to the cysteine facing away from the active center (CYS “out” state). A similar energy profile is observed in GapN Penta (Figure 2B). *Sm* GapN functions physiologically as a tetramer and the closely related *Thermoproteus tenax* GapN was found to exhibit discontinuous saturation kinetics implying subunit cooperativity regulated by allosteric effects.[33,34] The alternating CYS “in” versus “out” states among different monomers indicate that the simulation is able to capture the dynamic cooperativity.

In contrast to the wild type and GapN Penta, almost all monomers of GapN Hex prefer the 12 Å CYS “out” state (Figure 2C). The difference in the positioning of the catalytic cysteine suggests that the decrease in k_{cat} for NMN^+ in GapN Hex originates from the improper alignment of CYS 284 in the formation of the hemithioacetal intermediate. Furthermore, the allosteric cooperativity among monomers was not observed indicating disruption of global dynamics. None of the mutations in GapN Hex are near CYS 284 and obtaining a mechanistic basis for the change in flexibility required further analysis.

We analyzed the trajectories by calculating the dynamic cross correlation of alpha carbons between all residue pairs of the tetramer and from that computed the shortest path network. The shortest path algorithm allows us to examine how allosteric movement propagates in proteins.[35] The analysis for the wild type reveals an extensive network that extends into each of the monomers and the dynamical communication passes through the tetramer interface as shown by the larger spheres that represent the frequency score for path usage (Figure 3A). GapN Penta exhibits a decrease in the overall network connectivity, as well as a shift away from the tetramer interface toward intramonomer clustering resulting in an overall decrease in intermonomer pathway usage (Figure 3B). However, the more striking changes occur in GapN Hex, where there is a significant decrease in the number of residues, pathways, and range of the network. The communication across the tetramer interface is lost and

very limited dynamical communication is depicted (Figure 3C). Overall, network analysis suggests that GapN Hex may be catalytically impaired due to its inability to position CYS 284 for optimal catalytic alignment arising from allosteric effects driven by its overly rigid structure.

The most catalytically efficient design, GapN Penta, represents an ~45 and ~68-fold increase in the catalytic efficiency and turnover rate for NMN^+, respectively, compared to the wild type (Table 1). The results for GapN Hex demonstrate that rational designs increasing NMN^+ affinity should be carefully engineered to minimize disruption of flexibility, this may require compensatory mutations that are difficult to predict.

Engineering of an Orthogonal GapN.

GapN Penta, with its high turnover number, is well suited to cell-free biomanufacturing where crosstalk with other cofactors can be limited by providing high NMN^+ concentrations and low $NAD(P)^+$. However, for whole-cell biomanufacturing applications where specific electron shuttling from the EMP pathway to the target biotransformation is ideal, we required a GapN variant with minimal NAD^+ and $NADP^+$ activity at the physiologically relevant levels of these natural cofactors.

To assess the ability of our GapN variants to specifically reduce NMN^+, we sought to couple cell growth rate to GapN NMN^+ activity using growth as a facile readout for orthogonality.[13] This is achieved by replacing *E. coli*'s native glyceraldehyde-3-phosphate dehydrogenase (phosphorylating), encoded by *gapA*, with *Sm* GapN. A potential detour bypassing the GapN step in EMP glycolysis is also disrupted by knocking out the methylglyoxal synthase encoded by *mgsA* (Figure 4A).[36] We further disrupted the gene *pncC*, which encodes an NMN^+ amidohydrolase, to decrease degradation of exogenously supplied NMN^+.[13,37] In semi-defined media with glucose and casein amino acids, the final strain MX601 (Δ*gapA* Δ*mgsA*Δ*pncC*) grows poorly but is rescued by *Sm* GapN WT expression (Figure S4).

Although the catalytic activity toward $NADP^+$ is decreased by ~9300-fold in GapN Penta, in vivo studies of cells harboring GapN Penta still showed substantial growth in the absence of supplied NMN^+ (Figure 4B). Based on the kinetic parameters of GapN Penta (Table 1), we hypothesized that residual $NADP^+$ activity was restoring growth. In our previous efforts to engineer an NMN^+-orthogonal glucose dehydrogenase, we introduced negatively charged residues proximal to the AMP moiety to create electrostatic repulsion with the pyrophosphate group of NAD^+ and $NADP^+$ to disrupt binding while avoiding undesirable effects on NMN^+ binding.[13] Following the same design principle, we introduced the mutation G214E into the most active NMN^+ variants GapN Quad and GapN Penta. Although this strategy was found to be incompatible with GapN Penta due to potential steric clash with existing mutations (Figure S5A), it succeeded in GapN Quad resulting in GapN Ortho (P179K-F153S-S330R-I234E-G214E) and led to a ~21-fold decrease in $NADP^+$ activity while retaining ~70% of NMN^+ activity (Figure S5B,C). Introduction of G214E also decreased the specific activity for NAD^+ (Figure S5D).

The most orthogonal variant generated, GapN Ortho, exhibited decreased catalytic efficiency for $NADP^+$ and NAD^+ relative to the most active variant, GapN Penta (Table 1). GapN

Ortho features a 67- and 3.4 × 10^6-fold cofactor specificity switch compared to WT from NAD^+ and $NADP^+$ to NMN^+, respectively, based on catalytic efficiency. In particular, the large K_m of the enzyme for NAD^+ and $NADP^+$ falls far outside the physiological range of native cofactor concentrations in *E. coli*,[38] suggesting potential orthogonality in vivo. The mutations designed also impact D-G3P binding, leading to an increased apparent K_m for D-G3P from 0.22 ± 0.04 mM for GapN WT to 0.68 ± 0.1 mM for GapN Penta (Table 1). GapN Penta and GapN Ortho have similar effects on D-G3P binding, with increased K_m for D-G3P to 0.72 ± 0.1 mM for GapN Ortho (Table 1).

In vivo growth study of cells expressing GapN Ortho showed severely reduced growth without NMN^+ supplementation as *E. coli*'s preferred carbon source, glucose, could not be consumed by the EMP pathway. When 2 mM NMN^+ was supplemented in the media, GapN Ortho enabled robust growth, indicating that the EMP pathway was successfully rewired to be coupled to the NMN^+ concentration. In comparison, GapN Penta which retained vestigial NAD/P^+ activity displayed significant growth without NMN^+ which signaled insufficient orthogonality (Figure 4B). These results are the first demonstration of an EMP glycolysis in *E. coli* based on an orthogonal redox cofactor.

Elucidation of the Mechanism of Orthogonality.

To understand the marked cofactor specificity shift in GapN Ortho compared to other GapN variants, we performed Rosetta modeling to predict the binding poses of GapN wild type, GapN Penta, and GapN Ortho with NMN^+, NAD^+, and $NADP^+$. The negatively charged residue G214E in GapN Ortho forms a hydrogen bond with P179K when bound with $NADP^+$ and strengthens positioning of P179K to support an existing hydrogen-bond interaction with I234E (Figure 5A).

This emergent hydrogen bond network altered the hydrophobic surface required for packing against the adenine ring in $NADP^+$ (Figure S6) and additionally introduced steric clash to push the AMP moiety of $NADP^+$ out of the binding pocket (Figure 5B). The predicted binding pose is consistent with the apparent kinetic parameters. The catalytic efficiency of GapN Ortho toward $NADP^+$ decreases 50-fold from GapN Penta and 465,000-fold from GapN WT, respectively. On the other hand, the docked structures of GapN Ortho with NMN^+ show a similar binding mode to that observed with GapN Penta (Figure S6), consistent with the minimal disruption in NMN^+ activity.

A similar but less pronounced displacement is noticed with NAD^+ bound in GapN Ortho, where S330R serves as an extra anchor point for NAD^+ by interacting with the cofactor's adenosine ribose hydroxyl groups (Figure S6). This agrees with our findings that the catalytic efficiency of GapN Ortho is higher toward NAD^+ than $NADP^+$. Future engineering surrounding S330R may continue to improve orthogonality.

CONCLUSIONS

Designing enzymes to utilize noncanonical cofactors such as NMN^+ is challenging due to the lack of structural design principles and enormous sequence space that must be navigated. Current approaches rely on weakly guided searches where the template sequence

is perturbed and screened for fortuitous variants with high fitness, and the mechanistic contributions of the discovered mutations are unresolved. Here, we first demonstrate a Rosetta workflow sampling potential NMN^+ binding poses with mutated binding sites to provide design recommendations that enhance catalytic efficiency with NMN^+, this enables predictive design at low experimental costs (Table S2). We next perform molecular dynamics simulations of the tetrametric GapN variants to determine how the discovered mutations contribute to allosteric effects modulating the turnover rate and NMN^+ binding affinity. Our analysis indicates that the differences in kinetics are attributed to changes in backbone flexibility, displacement of the catalytic cysteine, and alterations to residue network connectivity. These complex and global effects observed in molecular dynamics simulations highlight the importance of high-throughput directed evolution, which can be performed in vivo with growth as a facile readout using our established NMN^+-dependent EMP pathway in *E. coli*.

METHODS

GapN Rational Design and Ligand Docking.

The crystal structure of *Sm* GapN (PDB: 1QI1) with D-G3P and $NADP^+$ bound was used for ligand docking and enzyme design.[20] Because 1QI1 harbored the mutation C284S, we first mutated it back to cysteine with the Rosetta Modeling Suite and relaxed the structure using a backbone constrained FastRelax procedure.[39] This pre-processed model was used for subsequent docking simulations and enzyme design. NMN^+ and NAD^+ conformer libraries were prepared according to previous research.[13] Generation of the $NADP^+$ conformer library is detailed in the Supporting Information. Initial coordinates for NMN^+ were obtained by removing the AMP moiety from $NADP^+$. For each docking or design simulation, the substrates of GapN, D-G3P, and one of the cofactors (NMN, NAD^+, and $NADP^+$) were placed into the active site and the enzyme–ligand complex was repacked and optimized. The Rosetta design protocol to identify amino acid substitutions predicted to improve binding affinity for NMN^+ consisted of rounds of Monte Carlo evaluation with moves randomly translating and rotating the NMN^+, sampling of alternative rotamers and side chain substitutions optimizing hydrophobic packing or polar contacts with NMN^+, and backbone minimization to relieve torsional strain and examine different binding pocket geometries. Design simulation was performed with the Rosetta EnzRepackMinimize mover. Distance and angle restraints were imposed to maintain the cofactors in catalytically competent geometry for hydride transfer in relation to CYS 284 and D-G3P. A total of 2000 simulations were run for each batch, the top 20 best scoring outputs sorted by constraint score, protein–ligand interface energy score, and total system energy score were selected for further optimization and design using Foldit Standalone.[40] Variants measured to have favorable Rosetta total energy and interface energy, the sum of hydrophobic and electrostatic interactions between the ligand and protein were selected for experimental validation. For ligand docking simulation, the protocol was the same except with design option = 0 (no design allowed) and the corresponding mutations were generated by applying the MutateResidue mover in Rosetta-Scripts. The example run files including constraints, options, RosettaScripts XML, and ligands params are included in the Supporting Information.

Molecular Dynamics Simulations.

The atomic coordinates for GapN WT, GapN Penta, and GapN Hex with NMN^+ were optimized through the Rosetta design protocol and the tetrameric structure was made using PDB ID: 1QI1 structure as a template. A simulation setup was created using the CHARMM-GUI web server.[41] The protein and ligands were modeled with the Amber ff19SB[42] and GAFF[43] force fields, and water was modeled using the modified TIP3P[44] model. The simulation box was set to 125 × 125 × 125 Å with 51,093 water molecules. The systems were neutralized with potassium and chloride ions and brought to 0.15 M physiological ionic concentrations. The Particle Mesh Ewald method[45] was used to treat the long-range electrostatic interactions and the short-range interactions were switched off at 10 Å. The systems were equilibrated for 40 picoseconds before the Orthogonal Space Tempering[46,47] (OST) production runs. The OST simulations were performed under the *NPT* ensemble with the temperature kept constant at 300 K using a Nose–Hoover thermostat[48] and the pressure kept constant at 1 atm using a Langevin piston barostat.[49] The SHAKE algorithm[50] was used to constrain all bonds containing hydrogen. The simulation timestep was set to 1 fs and the trajectory was saved every 2 ps for data analysis. The all-atom molecular dynamics simulation was performed on a customized version of CHARMM[51] that implements the OST enhanced sampling method. Production simulations were run for the GapN wild type, and the GapN Penta and GapN Hex mutants bound to NMN^+ for 800 ns simulation time using the Cα atoms for the RMSD order parameter. The variances of simulated free energies are below 0.5 kcal/mol. Analysis of trajectory data was performed with CPPTRAJ[52] and network analysis using Dynacomm.py script.[35]

Plasmid Construction.

Generated plasmids and strains are listed in Table S1. Plasmid construction was completed with the Gibson isothermal DNA assembly method. Site-directed mutagenesis was performed via PCR with PrimeSTAR Max DNA Polymerase (TaKaRa) and mutagenic primers carrying the target codon substitutions to amplify DNA fragments for ligation. Cloning steps were run with *E. coli* XLI-Blue (Stratagene). Plasmid isolation was carried out with the QIAprep Spin Miniprep Kit (Qiagen) and nucleotide sequences were validated by Sanger sequencing (Laragen).

The *S. mutans gapN* gene was amplified from a gBlock template (IDT DNA), cleaned through gel extraction, and inserted into the pQE vector backbone (N-terminal 6 × His-tag, ColE1 *ori*, and Amp^r) through a Gibson assembly to generate pEK-198. Plasmids encoding the mutants were built through site-directed mutagenesis on the pEK-198 template.

The *Pseudomonas putida xenA* gene was subcloned from a plasmid[13] with overlaps appropriate for Gibson isothermal assembly into a pRSF vector.

Media, Buffers, and Cultivation.

Detailed recipes for media and buffers are included in the Supporting Information. Routine culturing was done in 2 × YT media (except for PHL2 and MX601) with antibiotics at concentrations of 100 mg/L for ampicillin, 50 mg/L for spectinomycin, 50 mg/L for kanamycin, and 10 mg/L for tetracycline. Routine culturing of PHL2 and MX601 was

performed in succinate glycerol casein amino acids minimal medium (SGC) with the following composition: 1× M9 minimal media, 50 mM sodium succinate, 50 mM glycerol, and 0.1% (w/v) casein amino acids.

Strain Construction.

E. coli strain MX601 was constructed based on the PHL2 strain previously reported[36] and knockout of the *pncC* gene was conducted by P1 transduction[53] from the strain JW2670-1 (Δ*pncC* : kan) of the Keio collection.[54] Plasmid pCP20 was used to remove the kanamycin resistance marker after confirmation of the gene deletion. SGC media containing tetracycline was used to routinely culture the strain.

Protein Expression and Purification.

Proteins were expressed with a N-terminal 6 × His-tag for affinity purification with the His-Spin Protein Miniprep kit (Zymo Research Corporation). Plasmids were inserted into *E. coli* BL21 (DE3) by transformation for overexpression, transformant colonies were inoculated in 2 × YT media with 100 mg/L ampicillin for overnight expression, sub-cultured the next day at 1% volume with 100 mg/L ampicillin, induced with 0.5 mM IPTG at OD_{600} 0.5, and incubated at 30 °C for 24 h with 250 rpm shaking for protein production. Pelleted cells were disrupted with bead-beating and purification from the cell lysate was performed with a Ni-NTA resin according to manufacturer's protocols. Isolated proteins were quantified with a Bradford assay compared to a BSA standard curve and stored with 20% glycerol at −80 °C.

GapN Enzyme Assays.

The GapN enzyme assay protocol was adapted from previous works. The reactions to measure specific activities were initiated by the addition of purified enzyme into the assay mixture containing 50 mM Tris–Cl pH 8.5, 5 mM β-mercaptoethanol, 2 mM DL-G3P, and 4 mM cofactor at 25 °C. Production of reduced cofactor was detected with a spectrophotometer by absorbance at 340 nm. Final specific activities were corrected for cofactor carry-over during purification by subtracting the background activity measured from the reaction with no cofactor added.

Determination of the Michaelis–Menten kinetic parameters, k_{cat}, describing the turnover rate and Michaelis constant K_m was completed with a similar master mix, where DL-G3P was replaced with 1 mM D-G3P and cofactor concentration was varied. Initial reaction rates were recorded and fit to the Michaelis–Menten equation where v_0 is the initial velocity, E_t is the total enzyme concentration, and S is the cofactor concentration.

$$v_0 = \frac{E_t \cdot k_{cat} \cdot S}{K_m + S}$$

Under conditions where the enzyme could not be saturated with cofactor ($K_m \gg S$), the initial velocities were fit to the linear Michaelis–Menten equation to solve for catalytic efficiency k_{cat}/K_m.

$$v_0 = \frac{E_t \cdot k_{cat} \cdot S}{K_m}$$

Determination of kinetic parameters for D-G3P of GapN WT was conducted at 0.2 mM $NADP^+$ or 20 mM NMN^+. For kinetic parameters for D-G3P of GapN Penta, 5 mM $NADP^+$ or 20 mM NMN^+ was used. For GapN Ortho, 20 mM $NADP^+$ or 20 mM NMN^+ was used. When D-G3P inhibition was observed, initial reaction rates were recorded and fit to the Michaelis–Menten equation with substrate inhibition, where K_i is the dissociation constant of D-G3P at an inhibiting site on free enzyme and B is the D-G3P concentration.

$$v_0 = \frac{E_t \cdot k_{cat} \cdot B}{K_m + B \cdot \left(1 + \frac{B}{K_i}\right)}$$

NMN^+-Dependent Growth Restoration.

NMN^+-dependent growth restoration was performed as follows: plasmids pEK198, pEK253, pEK269, or pSM105 and pDA170 or pSM108 were introduced into competent cells prepared as detailed in the Supporting Information by electroporation. The cells were transferred from cuvettes by adding 200 μL SGC medium three times, rescued for 2 h at 37 °C, and then deposited on SGC agar plates containing antibiotics. After 24 h, three individual colonies were used to inoculate triplicate overnight cultures of 4 mL SGC with antibiotics. After 24 h, dense cell culture was used to inoculate 4 mL of SGC media to 0.1 OD_{600} and grown for 4.5 h at 30 °C ($OD_{600}$of 0.4–0.6). Cultures were induced by 0.5 mM IPTG and 0.1% (w/v) L-arabinose and then incubated shaking 4 h at 30 °C. Cultures were harvested and the volume necessary for a final resuspension at 2 OD_{600} in 1 mL was pelleted and washed three times with 1 mL M9 wash buffer at 8000 rpm for 2 min at room temperature. Washed cells resuspended in 1 mL M9 wash buffer were transferred to 3 mL growth challenge media (see the Supporting Information) with 0.05 starting OD_{600} containing variable NMN^+ concentrations in culture tubes and incubated shaking at 30 °C, 250 rpm.

Supplementary Material

Refer to Web version on PubMed Central for supplementary material.

ACKNOWLEDGMENTS

H.L. acknowledges support from the University of California, Irvine, the National Science Foundation (NSF) (award no. 1847705), and the National Institutes of Health (NIH) (award no. DP2 GM137427), Alfred Sloan Research Fellowship, and Advanced Research Projects Agency–Energy (ARPA-E) (award no. DE-AR0001508). Y.C. and J.B.S. acknowledge the funding of the National Institute of Environmental Health Sciences grant number: P42ES004699, the National Institutes of Health grant number R01 GM 076324-11, and the National Science Foundation grant numbers: 1627539, 1805510, and 1827246. R.L. acknowledges support from the National Institutes of Health (NIH) (award no. GM130367). D.A. acknowledges support from the NSF Graduate Research Fellowship Program (grant no. DGE1839285). S.M. acknowledges support from the NSF Graduate Research Fellowship Program (grant no. DGE1839285).

REFERENCES

1. Rasor BJ; Vögeli B; Landwehr GM; Bogart JW; Karim AS; Jewett MC Toward Sustainable, Cell-Free Biomanufacturing. Curr. Opin. Biotechnol 2021, 69, 136–144. [PubMed: 33453438]
2. Huisman GW; Liang J; Krebber A Practical Chiral Alcohol Manufacture Using Ketoreductases. Curr. Opin. Chem. Biol 2010, 14, 122–129. [PubMed: 20071211]
3. Rollin JA; Bomble YJ; St. John PC; Stark AK Biochemical Production with Purified Cell-Free Systems. Biochem. Eng. J 2021, 166, 107002.
4. Liu Y; Li Q; Wang L; Guo X; Wang J; Wang Q; Zhao ZK Engineering D-Lactate Dehydrogenase to Favor an Non-Natural Cofactor Nicotinamide Cytosine Dinucleotide. Chembiochem 2020, 21, 1972–1975. [PubMed: 32175634]
5. Nowak C; Pick A; Lommes P; Sieber V Enzymatic Reduction of Nicotinamide Biomimetic Cofactors Using an Engineered Glucose Dehydrogenase: Providing a Regeneration System for Artificial Cofactors. ACS Catal 2017, 7, 5202–5208.
6. Zachos I; Döring M; Tafertshofer G; Simon RC; Sieber V Carba Nicotinamide Adenine Dinucleotide Phosphate: Robust Cofactor for Redox Biocatalysis. Angew. Chem., Int. Ed 2021, 60, 14701–14706.
7. Wang L; Ji D; Liu Y; Wang Q; Wang X; Zhou YJ; Zhang Y; Liu W; Zhao ZK Synthetic Cofactor-Linked Metabolic Circuits for Selective Energy Transfer. ACS Catal 2017, 7, 1977–1983.
8. Guarneri A; Westphal AH; Leertouwer J; Lunsonga J; Franssen MCR; Opperman DJ; Hollmann F; Berkel WJH; Paul CE Flavoenzyme-mediated Regioselective Aromatic Hydroxylation with Coenzyme Biomimetics. ChemCatChem 2020, 12, 1368–1375.
9. Paul CE; Arends IWCE; Hollmann F Is Simpler Better? Synthetic Nicotinamide Cofactor Analogues for Redox Chemistry. ACS Catal 2014, 4, 788–797.
10. Campbell E; Meredith M; Minteer SD; Banta S Enzymatic Biofuel Cells Utilizing a Biomimetic Cofactor. Chem. Commun 2012, 48, 1898.
11. Rollin JA; Tam TK; Zhang Y-HP New Biotechnology Paradigm: Cell-Free Biosystems for Biomanufacturing. Green Chem 2013, 15, 1708.
12. Huang R; Chen H; Upp DM; Lewis JC; Zhang Y-HPJ A High-Throughput Method for Directed Evolution of NAD(P)+-Dependent Dehydrogenases for the Reduction of Biomimetic Nicotinamide Analogues. ACS Catal 2019, 9, 11709–11719. [PubMed: 34765284]
13. Black WB; Zhang L; Mak WS; Maxel S; Cui Y; King E; Fong B; Sanchez Martinez A; Siegel JB; Li H Engineering a Nicotinamide Mononucleotide Redox Cofactor System for Biocatalysis. Nat. Chem. Biol 2020, 16, 87–94. [PubMed: 31768035]
14. Richardson KN; Black WB; Li H Aldehyde Production in Crude Lysate- and Whole Cell-Based Biotransformation Using a Noncanonical Redox Cofactor System. ACS Catal 2020, 10, 8898–8903. [PubMed: 34306803]
15. Kay JE; Jewett MC A Cell-Free System for Production of 2,3-Butanediol Is Robust to Growth-Toxic Compounds. Metab. Eng. Commun 2020, 10, No. e00114. [PubMed: 31934547]
16. Valliere MA; Korman TP; Woodall NB; Khitrov GA; Taylor RE; Baker D; Bowie JU A Cell-Free Platform for the Prenylation of Natural Products and Application to Cannabinoid Production. Nat. Commun 2019, 10, 565. [PubMed: 30718485]
17. Opgenorth PH; Korman TP; Iancu L; Bowie JU A Molecular Rheostat Maintains ATP Levels to Drive a Synthetic Biochemistry System. Nat. Chem. Biol 2017, 13, 938–942. [PubMed: 28671683]
18. Sherkhanov S; Korman TP; Chan S; Faham S; Liu H; Sawaya MR; Hsu W-T; Vikram E; Cheng T; Bowie JU Isobutanol Production Freed from Biological Limits Using Synthetic Biochemistry. Nat. Commun 2020, 11, 4292. [PubMed: 32855421]
19. Rasor BJ; Yi X; Brown H; Alper HS; Jewett MC An Integrated in Vivo/in Vitro Framework to Enhance Cell-Free Biosynthesis with Metabolically Rewired Yeast Extracts. Nat. Commun 2021, 12, 5139. [PubMed: 34446711]
20. Cobessi D; Tête-Favier F; Marchal S; Branlant G; Aubry A Structural and Biochemical Investigations of the Catalytic Mechanism of an NADP-Dependent Aldehyde Dehydrogenase from Streptococcus Mutans. J. Mol. Biol 2000, 300, 141–152. [PubMed: 10864505]

21. Cobessi D; Tête-Favier F; Marchal S; Azza S; Branlant G; Aubry A Apo and Holo Crystal Structures of an NADP-Dependent Aldehyde Dehydrogenase from Streptococcus Mutans. J. Mol. Biol 1999, 290, 161–173. [PubMed: 10388564]
22. Ye X; Honda K; Sakai T; Okano K; Omasa T; Hirota R; Kuroda A; Ohtake H Synthetic Metabolic Engineering-a Novel, Simple Technology for Designing a Chimeric Metabolic Pathway. Microb. Cell Fact 2012, 11, 120.
23. Noor E; Bar-Even A; Flamholz A; Reznik E; Liebermeister W; Milo R Pathway Thermodynamics Highlights Kinetic Obstacles in Central Metabolism. PLoS Comput. Biol 2014, 10, No. e1003483. [PubMed: 24586134]
24. Park JO; Tanner LB; Wei MH; Khana DB; Jacobson TB; Zhang Z; Rubin SA; Li SH-J; Higgins MB; Stevenson DM; Amador-Noguez D; Rabinowitz JD Near-Equilibrium Glycolysis Supports Metabolic Homeostasis and Energy Yield. Nat. Chem. Biol 2019, 15, 1001–1008. [PubMed: 31548693]
25. Causey TB; Shanmugam KT; Yomano LP; Ingram LO Engineering Escherichia Coli for Efficient Conversion of Glucose to Pyruvate. Proc. Natl. Acad. Sci. U.S.A 2004, 101, 2235–2240. [PubMed: 14982993]
26. Koebmann BJ; Westerhoff HV; Snoep JL; Nilsson D; Jensen PR The Glycolytic Flux in Escherichia Coli Is Controlled by the Demand for ATP. J. Bacteriol 2002, 184, 3909–3916. [PubMed: 12081962]
27. Causey TB; Zhou S; Shanmugam KT; Ingram LO Engineering the Metabolism of Escherichia Coli W3110 for the Conversion of Sugar to Redox-Neutral and Oxidized Products: Homoacetate Production. Proc. Natl. Acad. Sci. U.S.A 2003, 100, 825–832. [PubMed: 12556564]
28. Zhu Y; Eiteman MA; Altman R; Altman E High Glycolytic Flux Improves Pyruvate Production by a Metabolically Engineered Escherichia Coli Strain. Appl. Environ. Microbiol 2008, 74, 6649–6655. [PubMed: 18806005]
29. Fleishman SJ; Leaver-Fay A; Corn JE; Strauch E-M; Khare SD; Koga N; Ashworth J; Murphy P; Richter F; Lemmon G; Meiler J; Baker D RosettaScripts: A Scripting Language Interface to the Rosetta Macromolecular Modeling Suite. PLoS One 2011, 6, No. e20161. [PubMed: 21731610]
30. Rahuel-Clermont S; Bchini R; Barbe S; Boutserin S; André I; Talfournier F Enzyme Active Site Loop Revealed as a Gatekeeper for Cofactor Flip by Targeted Molecular Dynamics Simulations and FRET-Based Kinetics. ACS Catal 2019, 9, 1337–1346.
31. D'Ambrosio K; Pailot A; Talfournier F; Didierjean C; Benedetti E; Aubry A; Branlant G; Corbier C The First Crystal Structure of a Thioacylenzyme Intermediate in the ALDH Family: New Coenzyme Conformation and Relevance to Catalysis. Biochemistry 2007, 46, 10234–10235.
32. Marchal S; Rahuel-Clermont S; Branlant G Role of Glutamate-268 in the Catalytic Mechanism of Nonphosphorylating Glyceraldehyde-3-Phosphate Dehydrogenase from Streptococcus Mutans. Biochemistry 2000, 39, 3327–3335. [PubMed: 10727225]
33. Lorentzen E; Hensel R; Knura T; Ahmed H; Pohl E Structural Basis of Allosteric Regulation and Substrate Specificity of the Non-Phosphorylating Glyceraldehyde 3-Phosphate Dehydrogenase from Thermoproteus Tenax. J. Mol. Biol 2004, 341, 815–828. [PubMed: 15288789]
34. Pohl E; Brunner N; Wilmanns M; Hensel R The Crystal Structure of the Allosteric Non-Phosphorylating Glyceraldehyde-3-Phosphate Dehydrogenase from the Hyperthermophilic Archaeum Thermoproteus Tenax. J. Biol. Chem 2002, 277, 19938–19945. [PubMed: 11842090]
35. Romero-Rivera A; Garcia-Borraś M; Osuna S Role of Conformational Dynamics in the Evolution of Retro-Aldolase Activity. ACS Catal 2017, 7, 8524–8532. [PubMed: 29226011]
36. Lin PP; Jaeger AJ; Wu T-Y; Xu SC; Lee AS; Gao F; Chen P-W; Liao JC Construction and Evolution of an Escherichia Coli Strain Relying on Nonoxidative Glycolysis for Sugar Catabolism. Proc. Natl. Acad. Sci. U.S.A 2018, 115, 3538–3546. [PubMed: 29555759]
37. Black WB; Aspacio D; Bever D; King E; Zhang L; Li H Metabolic Engineering of Escherichia Coli for Optimized Biosynthesis of Nicotinamide Mononucleotide, a Noncanonical Redox Cofactor. Microb. Cell Fact 2020, 19, 150. [PubMed: 32718347]
38. Bennett BD; Kimball EH; Gao M; Osterhout R; Van Dien SJ; Rabinowitz JD Absolute Metabolite Concentrations and Implied Enzyme Active Site Occupancy in Escherichia Coli. Nat. Chem. Biol 2009, 5, 593–599. [PubMed: 19561621]

39. Tyka MD; Keedy DA; André I; DiMaio F; Song Y; Richardson DC; Richardson JS; Baker D Alternate States of Proteins Revealed by Detailed Energy Landscape Mapping. J. Mol. Biol 2011, 405, 607–618. [PubMed: 21073878]
40. Kleffner R; Flatten J; Leaver-Fay A; Baker D; Siegel JB; Khatib F; Cooper S Foldit Standalone: A Video Game-Derived Protein Structure Manipulation Interface Using Rosetta. Bioinformatics 2017, 33, 2765–2767. [PubMed: 28481970]
41. Lee J; Cheng X; Swails JM; Yeom MS; Eastman PK; Lemkul JA; Wei S; Buckner J; Jeong JC; Qi Y; Jo S; Pande VS; Case DA; Brooks CL; MacKerell AD; Klauda JB; Im W CHARMM-GUI Input Generator for NAMD, GROMACS, AMBER, OpenMM, and CHARMM/OpenMM Simulations Using the CHARMM36 Additive Force Field. J. Chem. Theory Comput 2016, 12, 405–413. [PubMed: 26631602]
42. Tian C; Kasavajhala K; Belfon KAA; Raguette L; Huang H; Migues AN; Bickel J; Wang Y; Pincay J; Wu Q; Simmerling C Ff19SB: Amino-Acid-Specific Protein Backbone Parameters Trained against Quantum Mechanics Energy Surfaces in Solution. J. Chem. Theory Comput 2020, 16, 528–552. [PubMed: 31714766]
43. Wang J; Wolf RM; Caldwell JW; Kollman PA; Case DA Development and Testing of a General Amber Force Field. J. Comput. Chem 2004, 25, 1157–1174. [PubMed: 15116359]
44. Jorgensen WL; Chandrasekhar J; Madura JD; Impey RW; Klein ML Comparison of Simple Potential Functions for Simulating Liquid Water. J. Chem. Phys 1983, 79, 926–935.
45. Essmann U; Perera L; Berkowitz ML; Darden T; Lee H; Pedersen LG A Smooth Particle Mesh Ewald Method. J. Chem. Phys 1995, 103, 8577–8593.
46. Zheng L; Chen M; Yang W Random Walk in Orthogonal Space to Achieve Efficient Free-Energy Simulation of Complex Systems. Proc. Natl. Acad. Sci. U.S.A 2008, 105, 20227–20232. [PubMed: 19075242]
47. Zheng L; Yang W Practically Efficient and Robust Free Energy Calculations: Double-Integration Orthogonal Space Tempering. J. Chem. Theory Comput 2012, 8, 810–823. [PubMed: 26593343]
48. Nosé S A Unified Formulation of the Constant Temperature Molecular Dynamics Methods. J. Chem. Phys 1984, 81, 511–519.
49. Feller SE; Zhang Y; Pastor RW; Brooks BR Constant Pressure Molecular Dynamics Simulation: The Langevin Piston Method. J. Chem. Phys 1995, 103, 4613–4621.
50. Ryckaert J-P; Ciccotti G; Berendsen HJC Numerical Integration of the Cartesian Equations of Motion of a System with Constraints: Molecular Dynamics of n-Alkanes. J. Comput. Phys 1977, 23, 327–341.
51. Brooks BR; Brooks CL; Mackerell AD; Nilsson L; Petrella RJ; Roux B; Won Y; Archontis G; Bartels C; Boresch S; Caflisch A; Caves L; Cui Q; Dinner AR; Feig M; Fischer S; Gao J; Hodoscek M; Im W; Kuczera K; Lazaridis T; Ma J; Ovchinnikov V; Paci E; Pastor RW; Post CB; Pu JZ; Schaefer M; Tidor B; Venable RM; Woodcock HL; Wu X; Yang W; York DM; Karplus M CHARMM: The Biomolecular Simulation Program. J. Comput. Chem 2009, 30, 1545–1614. [PubMed: 19444816]
52. Roe DR; Cheatham TE PTRAJ and CPPTRAJ: Software for Processing and Analysis of Molecular Dynamics Trajectory Data. J. Chem. Theory Comput 2013, 9, 3084–3095. [PubMed: 26583988]
53. Thomason LC; Costantino N; Court DL E. Coli Genome Manipulation by P1 Transduction. Curr. Protoc. Mol. Biol 2007, 79, 1–8.
54. Baba T; Ara T; Hasegawa M; Takai Y; Okumura Y; Baba M; Datsenko KA; Tomita M; Wanner BL; Mori H Construction of Escherichia Coli K-12 in-Frame, Single-Gene Knockout Mutants: The Keio Collection. Mol. Syst. Biol 2006, 2, 2006.

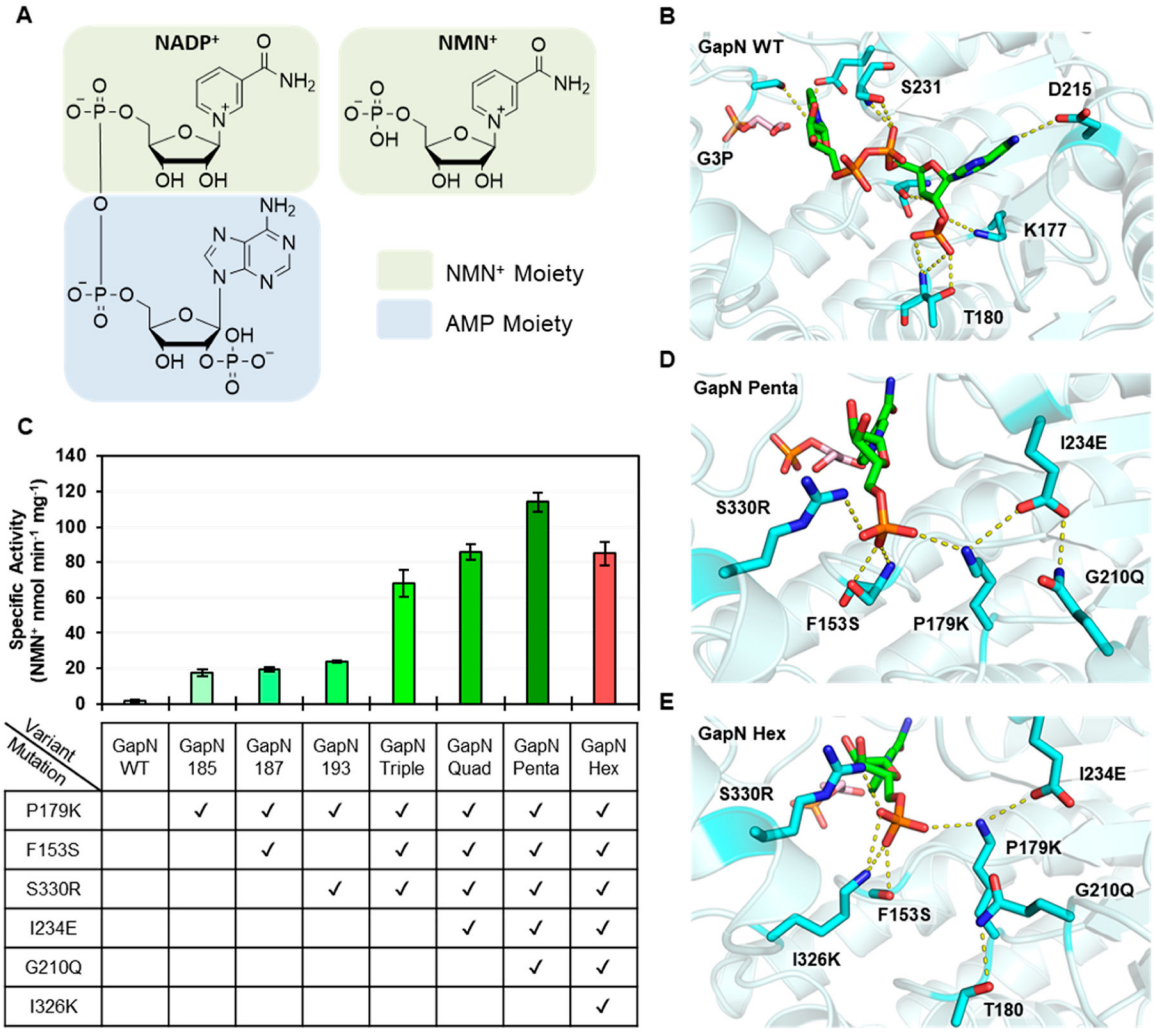

Variant / Mutation	GapN WT	GapN 185	GapN 187	GapN 193	GapN Triple	GapN Quad	GapN Penta	GapN Hex
P179K		✓	✓	✓	✓	✓	✓	✓
F153S			✓		✓	✓	✓	✓
S330R				✓	✓	✓	✓	✓
I234E						✓	✓	✓
G210Q							✓	✓
I326K								✓

Figure 1.

Rational engineering of *Sm* GapN to increase NMN^+ activity. (A) NMN^+ maintains the catalytic portion of $NAD(P)^+$ without the AMP moiety. (B) Cofactor binding interactions of GapN WT with its endogenous cofactor, $NADP^+$. (C) Specific activity of iteratively designed GapN variants. (D) Predicted cofactor binding interactions of GapN Penta with NMN^+ shows increasing polar and salt bridge contacts assisted by I234E and G210Q. (E) Predicted cofactor binding interactions of GapN Hex showing the additional salt bridge formed between NMN^+ phosphate and I326K that decreases both K_m and k_{cat}. Values are an average of at least three replicates ($n = 3$) with error bars of one standard deviation.

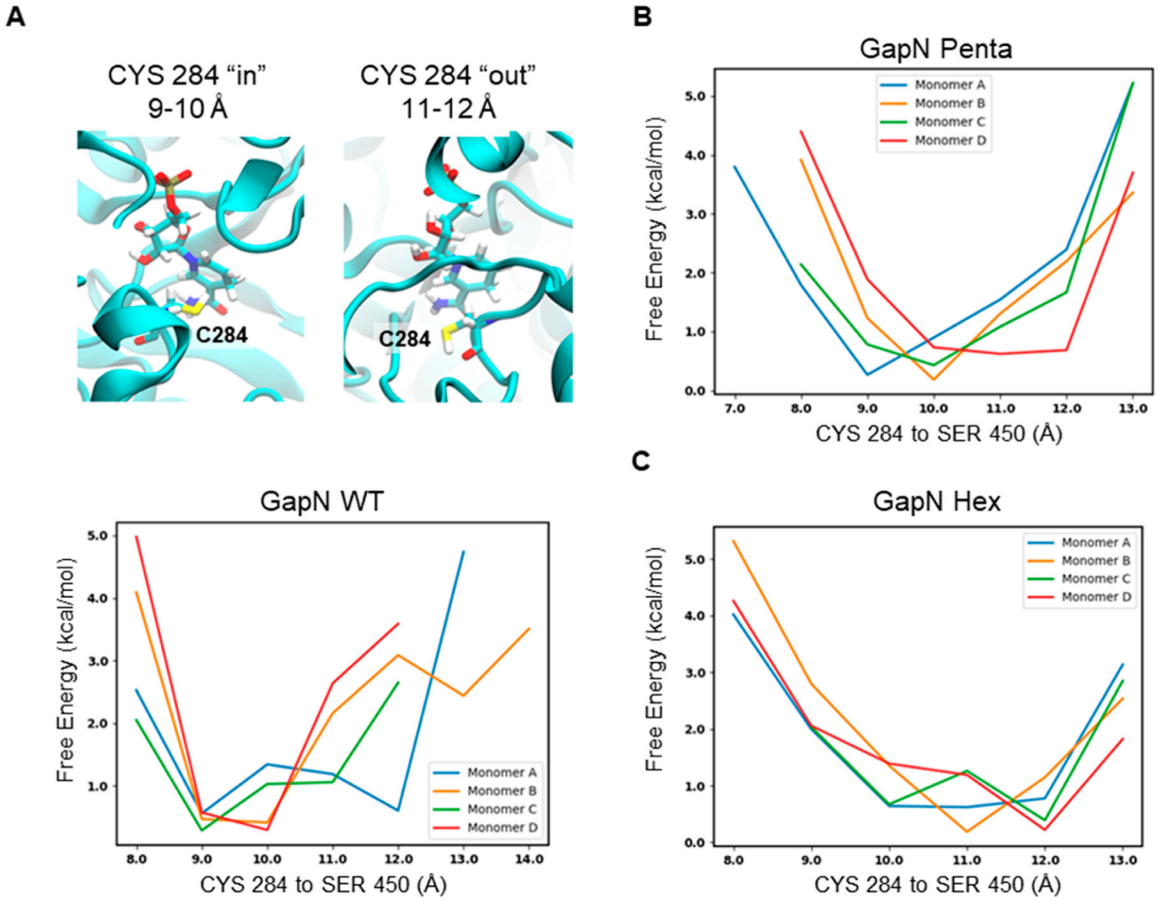

Figure 2.

Positioning of the catalytic CYS 284 in the wild type and mutants. (A) Free energy profiles of GapN WT display two distinct states. The positioning of the CYS 284 sulfhydryl is shown in representative models of the "in" and "out" states, corresponding to 9–10 and 12 Å distance between CYS 284 and SER 450, respectively. (B) Free energy profiles for each of the monomers in the GapN Penta mutant show similar CYS 284 positioning to GapN WT. (C) Free energy profiles of the GapN Hex variant deviates from GapN WT, with all monomers favoring the "out" state.

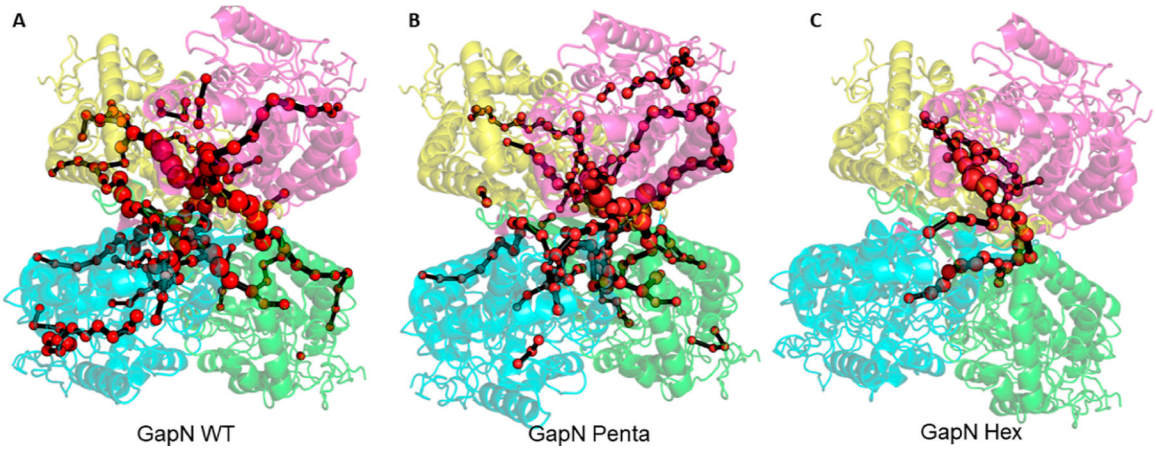

Figure 3.

Shortest path analysis of protein dynamical networks. The network shortest paths to the ligands are shown for (A) GapN WT and (B) GapN Penta with NMN^+ and (C) GapN Hex, which show the network by which allosteric movement propagates in proteins. The spheres along the path describe the frequency score which represents path usage for that alpha carbon. Significant decrease in allosteric communication is shown for GapN Hex, compared to the more catalytically capable WT and GapN Penta.

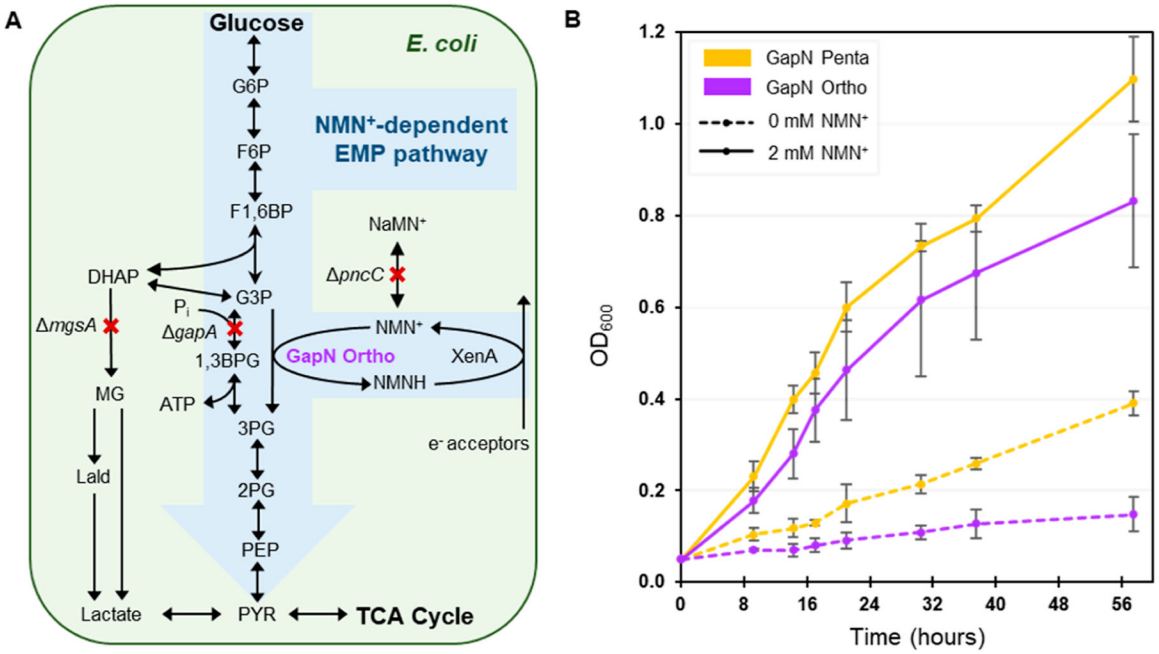

Figure 4.

GapN-dependent glycolysis as a facile evaluation of EMP pathway's orthogonality. (A) Engineered glycolysis in *E. coli* MX601 depends on GapN. (B) Growth of MX601 in semidefined media with 10 g/L glucose and 0.1% (w/v) casein amino acids. GapN Penta displays much higher growth than GapN Ortho in the absence of NMN^+, and both GapN variants support fast growth with 2 mM NMN^+ supplementation. Values are the average of biological triplicates ($n = 3$) with error bars representing one standard deviation. G6P, glucose 6-phosphate; F6P, fructose 6-phosphate; F1,6BP, fructose 1,6-bisphosphate; G3P, D-glyceraldehyde 3-phosphate; DHAP, dihydroxyacetone phosphate; MG, methylglyoxal; Lald, lactaldehyde; 1,3BPG, 1,3-bisphosphoglycerate; 3PG, 3-phosphoglyerate; 2PG, 2-phosphoglycerate; PEP, phosphoenolpyruvate; PYR, pyruvate; NMN^+, nicotinamide mononucleotide; $NaMN^+$, nicotinic acid mononucleotide; *pncC*, *E. coli* nicotinamide mononucleotide amidohydrolase; *mgsA*, *E. coli* methylglyoxal synthase; gapA, *E. coli* glyceraldehyde 3-phosphate dehydrogenase (phosphorylating); GapN, *S. mutans* glyceraldehyde 3-phosphate (nonphosphorylating); XenA, P. putida enoate reductase; and EMP, Embden–Meyerhof–Parnas.

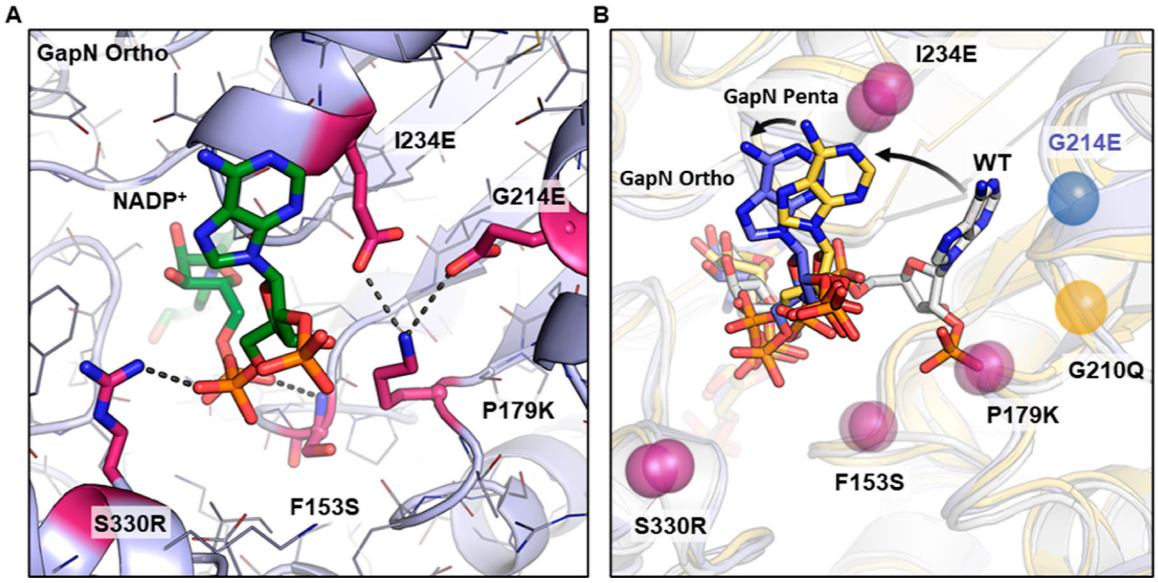

Figure 5.

Modeled structure of the most orthogonal variant GapN Ortho and its binding interactions with $NADP^+$. (A) Newly introduced mutation G214E on top of GapN Quad is predicted to form a hydrogen bond with residue P179K. The emergent interaction can reinforce the hydrogen bond interaction between I234E and P179K. The hydrogen bond network precludes the naturally favorable binding of AMP in $NADP^+$ by locking the residues in place to occupy the AMP pocket. (B) Predicted changes in $NADP^+$ binding pose in the wild type GapN (WT), GapN Penta (P179K-F153S-S330R-I234E-G210Q), and GapN Ortho (P179K-F153S-S330R-I234E-G214E). The corresponding mutations are highlighted in purple (P179K, F153S, S330R and I234E, shared by GapN Penta and GapN Ortho), blue (G214E, GapN Ortho exclusively) and yellow (G210Q, GapN Penta exclusively). Compared to WT, GapN Penta forces $NADP^+$ to bind in an unfavorable conformation with the AMP loosely held. G214E in GapN Ortho further moves $NADP^+$ from its native binding mode toward the solvent by occluding the AMP moiety. The AMP binding position is shifted from GapN WT, GapN Penta, and GapN Ortho mutations.

Table 1.

Apparent Kinetic Parameters of *Sm* GapN Variants[a]

Variant (Mutations)	Cofactor	k_{cat} (s^{-1})	K_m (mM)	k_{cat}/K_m (mM^{-1} s^{-1})
Apparent kinetic parameters for cofactor				
GapN WT	NAD^+	0.87 ± 0.01	8.3 ± 0.4	0.10
	$NADP^+$	19 ± 0.7	0.020 ± 0.001	930
	NMN^+	0.012 ± 0.001	8.1 ± 0.8	0.0015
GapN Penta (P179K-F153S-S330R-I234E-G210Q)	NAD^+	n.d.	n.d.	0.043 ± 0.001
	$NADP^+$	0.26 ± 0.01	2.6 ± 0.4	0.10
	NMN^+	0.82 ± 0.1	12 ± 4	0.067
GapN Hex (P179K-F153S-S330R-I234E-G210Q-I326K)	NAD^+	n.d.	n.d.	0.012 ± 0.001
	$NADP^+$	0.18 ± 0.01	1.1 ± 0.1	0.17
	NMN^+	0.12 ± 0.01	5.0 ± 0.7	0.025
GapN Ortho (P179K-F153S-S330R-I234E-G214E)	NAD^+	0.021 ± 0.001	2.0 ± 0.1	0.011
	$NADP^+$	0.016 ± 0.001	8.3 ± 1	0.0020
	NMN^+	0.081 ± 0.001	7.7 ± 0.2	0.011

Variant (mutations)	Cofactor	k_{cat} (s^{-1})	K_m (mM)	K_i (mM)	k_{cat}/K_m (mM^{-1} s^{-1})
Apparent kinetic parameters for D-G3P					
GapN WT	$NADP^+$	n.d.	n.d.	n.a.	5.5 ± 0.9
	NMN^+	0.025 ± 0.001	0.22 ± 0.04	1.9 ± 0.3	0.12 ± 0.02
GapN Penta (P179K-F153S-S330R-I234E-G210Q)	$NADP^+$	0.25 ± 0.01	0.78 ± 0.04	0.97 ± 0.02	0.32 ± 0.02
	NMN^+	0.65 ± 0.06	0.68 ± 0.1	1.3 ± 0.1	0.95 ± 0.2
GapN Ortho (P179K-F153S-S330R-I234E-G214E)	$NADP^+$	0.021 ± 0.001	0.036 ± 0.007	n.a.	0.58 ± 0.1
	NMN^+	0.28 ± 0.03	0.72 ± 0.1	1.6 ± 0.2	0.40 ± 0.08

[a]Reactions for the determination of cofactor kinetic parameters were performed with 50 mM Tris–Cl pH 8.5, 5 mM β-mercaptoethanol, 1 mM D-G3P, and varying cofactor concentrations at 25 °C. Reactions for determination of D-G3P kinetic parameters were performed with 50 mM Tris–Cl pH 8.5, 5 mM β-mercaptoethanol, varying D-G3P, and fixed cofactor concentrations at 25 °C. For parameters marked "n.d.", the enzyme could not be saturated within the range of cofactor concentrations tested. Therefore, data was fit to a simplified form of the Michaelis–Menten equation as described in methods. For combinations where D-G3P inhibition was not observed, inhibition constant, K_i, is marked as not applicable, "n.a.". The max D-G3P concentration tested was 4 mM. Values after ± represent one standard deviation of at least three replicates ($n = 3$).